Actomyosin-mediated inhibition of synaptic vesicle release under CB1R activation

Maureen H Mcfadden, Michel-Boris Emeritt, Hao Xu, Yihui Cui, Christophe Leterrier, Diana Zala, Laurent Venance, Zsolt Lenkei

ARTICLE OPEN

Check for updates

Actomyosin-mediated inhibition of synaptic vesicle release under CB_1R activation

Maureen H. McFadden[1,2,6], Michel-Boris Emeritt[3,6], Hao Xu[4,6], Yihui Cui[4], Christophe Leterrier[5], Diana Zala[2,3], Laurent Venance[4] and Zsolt Lenkei[2,3]✉

Long-term synaptic plasticity is critical for adaptive function of the brain, but presynaptic mechanisms of functional plasticity remain poorly understood. Here, we show that changes in synaptic efficacy induced by activation of the cannabinoid type-1 receptor (CB_1R), one of the most widespread G-protein coupled receptors in the brain, requires contractility of the neuronal actomyosin cytoskeleton. Specifically, using a synaptophysin-pHluorin probe (sypH2), we show that inhibitors of non-muscle myosin II (NMII) ATPase as well as one of its upstream effectors Rho-associated kinase (ROCK) prevent the reduction of synaptic vesicle release induced by CB_1R activation. Using 3D STORM super-resolution microscopy, we find that activation of CB_1R induces a redistribution of synaptic vesicles within presynaptic boutons in an actomyosin dependent manner, leading to vesicle clustering within the bouton and depletion of synaptic vesicles from the active zone. We further show, using sypH2, that inhibitors of NMII and ROCK specifically restore the release of the readily releasable pool of synaptic vesicles from the inhibition induced by CB_1R activation. Finally, using slice electrophysiology, we find that activation of both NMII and ROCK is necessary for the long-term, but not the short-term, form of CB_1R induced synaptic plasticity at excitatory cortico-striatal synapses. We thus propose a novel mechanism underlying CB_1R-induced plasticity, whereby CB_1R activation leads to a contraction of the actomyosin cytoskeleton inducing a reorganization of the functional presynaptic vesicle pool, preventing vesicle release and inducing long-term depression.

Translational Psychiatry (2024)14:335 ; https://doi.org/10.1038/s41398-024-03017-4

INTRODUCTION

The cannabinoid type-1 receptor (CB_1R) is a G-protein coupled receptor (GPCR) known widely to mediate the psychoactive effects of cannabinoids such as THC. As part of the neuromodulatory endocannabinoid system, it is also a key player in the endogenous regulation of mood, appetite, and pain perception, and has long been considered as a target of therapeutic treatment for various disorders including multiple sclerosis and epilepsy [1, 2]. How CB_1R can regulate these effects at the neuronal level is mainly attributed to the known forms of synaptic plasticity induced by its activation. Indeed, activation of CB_1R is known to lead to both short-term depression (STD) and long-term depression (LTD) of synaptic transmission [3], whereby activation of CB_1R at the presynaptic terminal decreases transmission during neuronal activity by inhibiting synaptic vesicle (SV) release. By affecting synaptic plasticity, CB_1R can affect the computations of multiple neural networks, leading to changes in behavioral outputs ranging from cognition to fine movement control and emotional regulation, as it is not only highly expressed in both the limbic system and cerebellum, but also present throughout the cortex [4–6].

Like other mechanisms of presynaptic plasticity, how CB_1R activation may lead to inhibition of release during long-term plasticity remains poorly understood. This paucity in knowledge stems partly from the complexity of the molecular interactions required for synaptic vesicle exocytosis and recycling, essential steps in neurotransmission. However, recent studies have started to shed light on the mechanisms that might be at play. In particular, CB_1R activation leads to a decrease in synaptic vesicles docked at the active zone (AZ), observed with electron microscopy both at hypoglossal terminals [7] and at cerebellar granule cell synapses [8, 9]; a recent study finds opposite effects in human cultured neurons [10]. Nonetheless, an increase in docked vesicles was reported in CB_1R-KO mice [11], suggesting CB_1R plays a role in regulating SV pool distribution. CB_1R-induced synaptic depression may thus result from a depletion of docked synaptic vesicles from the active zone (AZ). However, although these studies provide a structural mechanism explaining the prevention of SV release under CB_1R, a direct molecular pathway tying CB_1R activation to SV redistribution remains debated.

An additional difficulty in the study of GPCR-induced mechanisms stems from the complexity of G-protein subunit molecular interactions, known to interact directly or indirectly with countless downstream effectors. CB_1R has typically been reported to interact with the main inhibitory G protein pathway associated to $G_{i/o}$ [3], known to inhibit the cAMP/PKA molecular pathway. However, how inhibition of this pathway may prevent vesicle release

[1]Institut Pasteur, Université Paris Cité, Synapse and Circuit Dynamics Laboratory, CNRS UMR 3571, Paris, France. [2]Brain Plasticity Unit, ESPCI Paris, PSL Research University, CNRS, Paris, France. [3]Institute of Psychiatry and Neuroscience of Paris (IPNP), Université Paris Cité, INSERM U1266, Paris, France. [4]Dynamics and Pathophysiology of Neuronal Networks Team, Center for Interdisciplinary Research in Biology (CIRB), Collège de France, CNRS, INSERM, Université PSL, Paris, France. [5]NeuroCyto, Aix Marseille Université, CNRS, INP UMR 7051, Marseille, France. [6]These authors contributed equally: Maureen H. McFadden, Michel-Boris Emeritt, Hao Xu. ✉email: zsolt.lenkei@inserm.fr

Received: 6 February 2024 Revised: 16 April 2024 Accepted: 8 July 2024
Published online: 21 August 2024

remains to be determined. Several studies have also shown recruitment of the actomyosin cytoskeleton and its upstream activators under CB_1R during neural development [12–14]. We have previously shown this same pathway recruited downstream of CB_1R through $G_{12/13}$ recruitment during axonal pathfinding [14]. Furthermore, pharmacological stabilization of actin filaments impairs CB_1R-LTD in the hippocampus [15], suggesting that preserving the dynamics of the actomyosin cytoskeleton may be essential in CB_1R-induced effects at mature synapses.

Increasing evidence is bringing to light a role for the actomyosin cytoskeleton in the regulation of synaptic vesicle release. Disruption of the actin cytoskeleton has been found to prevent recovery of the readily releasable synaptic vesicle pool (RRP) under high frequency stimulation without affecting release under low frequency stimulation [16–20], suggesting actin filaments may be necessary to preserve SV repletion from the reserve pool. Emphasizing this hypothesis, depolymerization of the actin cytoskeleton has been found to increase vesicle mobility within presynaptic terminals [21, 22] and stabilization of the cytoskeleton can prevent relocation of SVs to the AZ [23], to inhibit vesicle cycling [24], and to reduce sustained vesicle release during prolonged stimulation [23, 25]. Recruitment of actomyosin by CB_1R may therefore explain the effects of CB_1R on vesicle depletion from the AZ, although this link has not yet been explored.

Here, we investigated the role of non-muscle myosin II (NMII), the main myosin protein responsible for the contraction of the actin cytoskeleton in non-muscle cells, on three of the established effects of CB_1R at the synapse: redistribution of synaptic vesicles, inhibition of SV release and synaptic plasticity. We found that the inhibition of SV release, and, more specifically, release of the readily releasable pool (RRP) of vesicles, under CB_1R activation is dependent on both NMII and one of its direct upstream effectors, Rho-associated protein kinase (ROCK). By imaging clusters of the vesicular protein VAMP2 at presynaptic boutons with STORM super-resolution microscopy, we show that SV distribution is altered upon CB1R activation and that this redistribution is prevented under inhibition of NMII. Finally, we found that both NMII and ROCK inhibition prevent excitatory CB_1R-LTD at cortico-striatal synapses, without impacting short-term plasticity, suggesting a ROCK/NMII dependent mechanism of SV redistribution during CB_1R-induced long-term plasticity.

RESULTS

NMII and ROCK inhibition prevent the reduction of vesicle release induced by CB1R activation

We first tested the influence of the actomyosin cytoskeleton on CB_1R-induced inhibition of SV cycling by using synaptophysin-pHluorin (sypH2) [26, 27], a pH-sensitive GFP variant tagged to the intra-vesicular domain of synaptophysin, and an established reporter of SV release. SypH2 was transfected into primary hippocampal cultures and release was imaged at 15-20 days in order to image mature synapses.

Sustained depolarization (2 min) of neurons with high concentrations of potassium chloride (KCl – 50 mM) induced a significant increase in fluorescence as compared to baseline (Fig. 1A–C), indicating vesicle cycling. Furthermore, alkalinizing intracellular compartments with ammonium chloride (NH_4Cl – 50 mM) induced a compounded increase in fluorescence, relating to the total pool of vesicles within the axonal bouton (Fig. 1A, B). Measuring the fluorescence increase after addition of KCl as a percentage of the

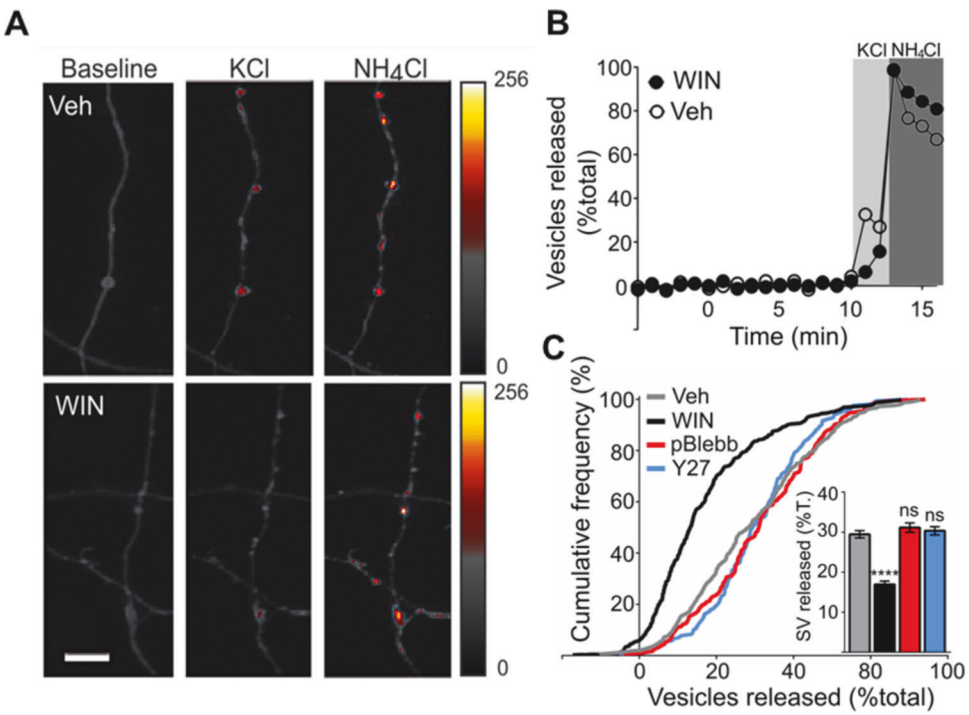

Fig. 1 Actomyosin contractility mediates cannabinoid-induced suppression of vesicle release. A Neuron expressing the vesicle release marker sypH2. Example SypH2 fluorescence levels in a control (Veh) and a WIN55,212-2-treated (WIN, 1 µM; 10 min) axon before stimulation (Baseline), after stimulation (KCl, 50 mM, 2 min), and after terminal superfusion with NH_4Cl (50 mM, 2 min). Fluorescence intensity (arbitrary units) increases during stimulation in control conditions while WIN decreases this effect. **B** Experimental paradigm and example traces of normalized axonal bouton SypH2 fluorescence **C** Cumulative probability distributions of the released vesicle pool fractions under control conditions (±0.92%; n = 337 over 4 independent experiments), or after treatment with WIN: (16.94 ± 0.84%; n = 323 over 4 independent experiments; P < 0.0001), pBlebb+WIN: (pBlebb: 25 µM; 20 min; 31.14 ± 1.15%; n = 173 over 3 independent experiments; P < 0.0001); Y-27632 + WIN (Y27: 10 µM; 20 min; 30.35 ± 1.03%; n = 168 over 3 independent experiments; P < 0.0001;. ****p < 0.001); ns not significant as compared to vehicle, Kruskal–Wallis test. Scale bar: 5 µm.

fluorescence peak after alkalinization gave us a measure of the fraction of vesicles released upon sustained depolarization. In our paradigm, this fraction was on average about 30% of the total pool (29.47 ± 1.81% – Fig. 1B, C), which scales well with other studies having used similar paradigms [28, 29], as well as measures of recycling pool sizes [30].

Bath application of the CB_1R selective agonist WIN55,212-2 (WIN – 1 μM) for 10 min prior to depolarization significantly reduced the fraction of vesicles released (Fig. 1A–C) (16.94 ± 1.67%; $p < 0.0001$). To test the role of actomyosin contractility in this effect, we applied the light-resistant form of blebbistatin, para-nitroblebbistatin (pBlebb – 25 μM), a selective non-muscle myosin II (NMII)-ATPase inhibitor [31], to our paradigm. pBlebb prevented CB_1R -induced inhibition when applied with the CB_1R agonist (Fig. 1C), indicating that contractility of the actomyosin cytoskeleton is implicated in the inhibition of vesicle cycling under CB_1R activation.

To further probe the link between CB_1R and NMII, we chose to inhibit the RhoA associated kinase ROCK, one of the kinases capable of activating NMII through phosphorylation of its myosin light chain (MLC) [32], and which was shown to be recruited by CB_1R during axonal pathfinding [13, 14]. Pretreatment with the ROCK selective inhibitor Y27632 (Y27 – 10 μM) significantly prevented the inhibition of vesicle cycling after CB_1R activation (Fig. 1C). Taken together these results provide evidence towards both the recruitment of the actomyosin cytoskeleton under CB_1R activation at mature synapses and the involvement of the actomyosin cytoskeleton in the effects of CB_1R on the inhibition of synaptic activity.

CB_1R activation does not affect AZ and post-synaptic density (PSD) size

SV release requires a series of complex mechanisms leading to the recruitment of SV to the AZ, exocytosis of SV for release of neurotransmitters and endocytosis of vesicles for replenishment of the SV pool [33]. Interruption of any of these stages would result in a reduction of sustained release. Although our sypH2 assay shows that the actomyosin cytoskeleton plays a role in preventing synaptic vesicle release under CB_1R activation, it does not allow us to determine which stage of the SV cycle is affected.

Prolonged activation of CB_1R has been found to reduce the size of presynaptic AZs [15]. A reduction in the size of the AZ could potentially induce a reduction in the number of SV release sites which would lead to a reduction of SV available for release. Therefore, we first chose to test the effect of CB_1R activation on synaptic morphology in our paradigm. We treated neuron cultures with either a DMSO vehicle or the CB_1R agonist WIN for 10 min. Neurons were then fixed and stained for both the presynaptic AZ scaffolding protein Bassoon and the excitatory PSD scaffolding protein Homer1 as a postsynaptic reference (Fig. 2A). We then imaged neurons using 2-color 3D Stochastic Optical Reconstruction Microscopy (STORM) [34], which allows for high resolution imaging below 50 nm resolution, allowing for more precise measurement of subsynaptic structures relative to conventional microscopy. Synapses positive for both Bassoon and Homer1 were selected visually along neuronal dendrites identified in reconstructed STORM images (Fig. 2A). Appositions were then clustered through DBSCAN clustering of the 3D STORM coordinates for each channel, and the size of each apposition was estimated by fitting an ellipsoid to the coordinates of the identified clusters (Fig. 2B).

Using this method, we found that AZ size, as determined by the spread of Bassoon staining, did not significantly differ between vehicle and WIN treated neurons, neither in length (Veh: $n = 11$, 460 ± 25 nm; WIN: $n = 8$, 500 ± 25 nm; $p = 0.539$) nor in total area (Fig. 2C). Homer1 spread did not change either with treatment (Fig. 2C), indicating no significant change in PSD size from CB_1R activation, which was expected due to the presynaptic locus of CB_1R. Thus, it is unlikely that the inhibition of release induced by CB_1R activation as seen in our paradigm is due to structural modification of the AZ.

Actomyosin contraction under CB_1R redistributes SV within boutons. As described previously, a redistribution of synaptic vesicles within axonal bouton terminals has been shown following both CB_1R activation [7–10] and disruption of the actin cytoskeleton [21–23]. By inducing a contraction of the actomyosin cytoskeleton, it is therefore possible that NMII activation through CB_1R could induce SV redistribution away from the AZ, preventing vesicle availability during release.

In order to investigate SV distribution under CB_1R activation in our paradigm, we chose to count the number of SVs close to the AZ by imaging vesicles immuno-stained with the vesicular SNARE protein VAMP2 with 3D STORM. VAMP2 has been estimated to have one of the highest copy numbers per vesicles [35] relative to other vesicular proteins, making it appropriate in the localization of individual vesicles in our paradigm.

We first attempted to stain both VAMP2 and Bassoon, as a reference for AZ scaffolding. However, imaging simultaneously both Bassoon and VAMP2 yielded a considerable amount of crosstalk between the two imaged channels, likely due to both cross-activation of closely positioned activation and emitter dyes as well as mis-registration of STORM localizations from opposing channels. This cross-talk made it impossible to distinguish Bassoon clusters from VAMP2 stained vesicles (data not shown).

As pre- and post-synaptic compartments have to be precisely aligned in order to ensure sensitive and efficient detection of synaptic events [36], the sizes of AZ and PSD synaptic scaffoldings tend to be highly correlated [37], suggesting that AZ location may be precisely predicted from the position of the PSD scaffold. In order to verify this empirically, we measured the length, width, and depth of Homer1 and Bassoon appositions using the principal axes of ellipsoids fitted to Homer1 and Bassoon (Fig. 2D, E; Supplementary Methods). All parameters were significantly correlated between corresponding appositions (Fig. 2D, E). This size relationship was not affected by CB_1R activation, as Bassoon to Homer1 length and width ratios did not differ with WIN treatment (Fig. 2D, E). Furthermore, distances between Homer1 and Bassoon appositions varied very little between synapses and were not affected under CB_1R activation with WIN. Based on these properties, we were successfully able to infer the nanoscale 3D location of the presynaptic AZ volume (Fig. 2F) based on postsynaptic Homer1 clusters. Indeed, on an independent sample, 95% of Bassoon locations were contained within our predicted AZ volume on average over all appositions tested (Fig. 2G).

We therefore applied this method to estimate the number of SV proximate to the active zone. Neuronal cultures were immunolabeled with both VAMP2 and Homer1 as a PSD/AZ reference (Fig. 3A; Supplementary Methods). VAMP2/Homer1 positive synapses were visually selected along identified dendrites (Fig. 3A) and pre- and post-synaptic appositions were clustered using DBSCAN as aforementioned (Fig. 3B; Supplementary Methods). VAMP2 labeled vesicles were then automatically identified within presynaptic bouton clusters by automating a nested version of our clustering algorithm (Fig. 3B; Supplementary Methods). SV identified in this manner over 59 boutons had a mean diameter of 67 nm (±8 nm) per bouton. This average diameter is above the localization uncertainty expected from single protein localization with our imaging resolution (<50 nm), and corresponds well to the diameter expected from the length added by primary and secondary antibodies (about 15 nm each) to a 30 nm vesicle, suggesting the structures identified with VAMP2 staining were indeed synaptic vesicles. By identifying SV in this manner, and estimating the AZ location using Homer1, we were able to count the number of SV proximal to the AZ under different treatment conditions (Fig. 3B–F). While total SV number did not significantly differ between treatments (Fig. 3C), we strikingly found fewer SV in the estimated

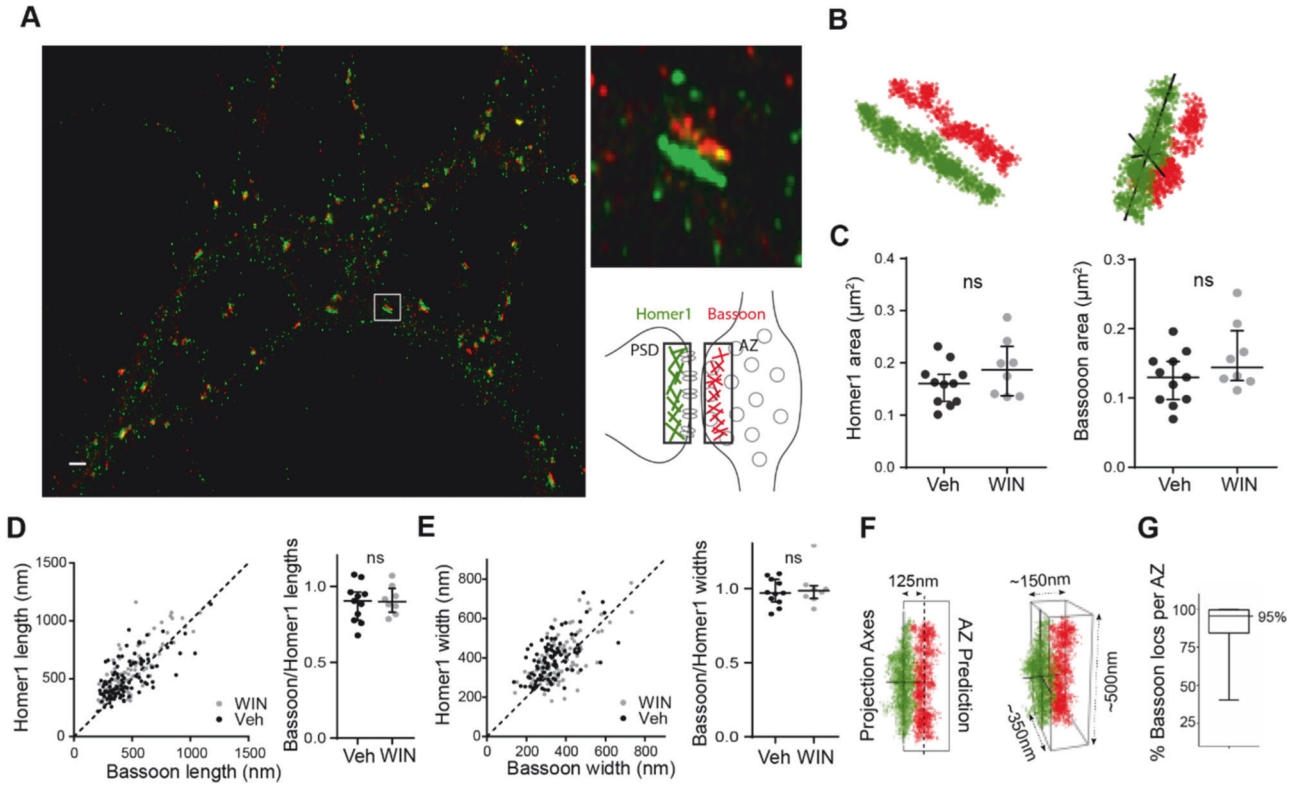

Fig. 2 STORM imaging shows CB_1R activation does not affect pre- or post-synaptic scaffolding ultrastructure. A STORM reconstruction of the pre-synaptic scaffolding protein Bassoon (red) and the post-synaptic scaffolding protein Homer1 (green) in cultured hippocampal neurons. Scale bar: 1 µm Top right: magnified image of the synapse squared on the left, bottom right: Cartoon showing synaptic locations of Bassoon and Homer1. **B** Left: Bassoon (red) and Homer1 (green) synaptic appositions of the synapse shown in A identified with DBSCAN clustering. Right: 3D angled view of the same synapse showing the axes resulting from 3D ellipsoid fitting of Homer1 localizations. **C** Mean Bassoon and Homer1 cluster areas per neuron for control (Veh) or after CB_1R activation (WIN). CB_1R activation did not have a significant effect on either Homer1 (Veh: 0.159 ± 0.012 µm^2, $n = 11$; WIN: 0.189 ± 0.019 µm^2, $n = 8$; $p = 0.236$, Mann–Whitney test) or Bassoon (Veh: 0.128 ± 0.011 µm^2, $n = 11$; WIN: 0.16 ± 0.017 µm^2, $n = 8$; $p = 0.205$, Mann–Whitney test) area. **D** Left: Homer1 versus Bassoon cluster lengths per synapse. Homer1 length is strongly correlated to Bassoon length both in control (Veh: $n = 105$, Spearman's rho $= 0.6165$, 95% confidence interval: 0.478-0.726; $p < 0.0001$) and WIN treated synapses (WIN: $n = 100$, Spearman's rho $= 0.755$, 95% confidence interval: 0.6517–0.830; $p < 0.0001$). Right: Mean ratio of Bassoon over Homer1 cluster lengths per neuron under control and WIN treatment conditions. CB_1R activation does not alter the ratio of Bassoon versus Homer1 lengths (Veh: $n = 11$, 0.891 ± 0.038; WIN: $n = 8$, 0.91 ± 0.033; $p = 0.891$, Mann–Whitney test). **E** Left: Homer1 versus Bassoon cluster widths per synapse. Homer1 width is strongly correlated to Bassoon length both in control (Veh: $n = 105$, Spearman's rho $= 0.557$, 95% confidence interval: 0.404–0.68; $p < 0.0001$) and WIN treated synapses (WIN: $n = 100$, Spearman's rho $= 0.594$, 95% confidence interval: 0.445–0.711; $p < 0.0001$). Right: Mean ratio of Bassoon over Homer1 cluster widths per neuron under control and WIN treatment conditions. CB_1R activation does not alter the ratio of Bassoon versus Homer1 widths (Veh: $n = 11$, 0.976 ± 0.027; WIN: $n = 8$, 1.00 ± 0.045; $p = 0.891$, Mann–Whitney test). **F** Example of an AZ prediction volume at an individual synapse. Left: Side-view of the synapse, showing the fitted axes (projection axes) and the estimated AZ location for that synapse (AZ prediction). Projection distance (125 nm) is based on the median measured distance between Bassoon and Homer1 appositions for all analyzed synapses. Right: angled view of the same synapse showing the 3D prediction volume. **G** Percentage of Bassoon localizations contained within the predicted AZ per synapse ($n = 55$, median: 95.5%; 25th percentile: 84.3%; 75th percentile: 99.4%). AZ active zone, PSD post-synaptic density, Bsn Bassoon, ns not significant.

AZ volume under WIN treatment, whereas pretreatment with pBlebb significantly prevented this effect (Fig. 3A), indicating that actomyosin contraction is necessary for depletion of AZ vesicles during CB_1R activation.

The actomyosin cytoskeleton is distributed throughout the presynaptic terminal [24, 38, 39] where it binds to SV via synapsin [38, 39]. As such, it is possible that contraction of the actomyosin cytoskeleton may lead to a clustering of synapsin-tethered vesicles within the bouton and away from the AZ, preventing release. Indeed, deletion of synapsin has previously been shown to reduce SV clustering within presynaptic terminals [40–42], and CB_1R has recently been found to promote the actin-bound form of synapsin in hippocampal synapses, along with increasing vesicle clustering within terminals [10]. We therefore tested whether actomyosin contraction under CB_1R activation could affect clustering of vesicles within boutons. To do this, we looked at nearest neighbor distances between SV in each treatment condition (Fig. 3F–H). We found that for increasing neighbors, up to the 12th nearest, SV were further apart under control conditions than under WIN (Fig. 3G), indicating increased clustering of vesicles under CB_1R activation. By comparing the median distance of each vesicle to its 12th nearest neighbor, we found that in boutons treated with WIN, SVs were significantly regrouped as compared to control (Fig. 3F–H). To avoid a potential effect of differences in SV number between different boutons biasing our results, we further normalized these distances by the density-based radius expected for each bouton under a uniform distribution of SV (Supplementary Methods). This normalization did not affect the clustering effect observed under WIN treatment as compared to control (Fig. 3H), indicating the vesicle clustering observed in this condition is due to an active regrouping of vesicles within boutons by CB_1R-activation, regardless of bouton size or total SV number. Furthermore, this effect was prevented

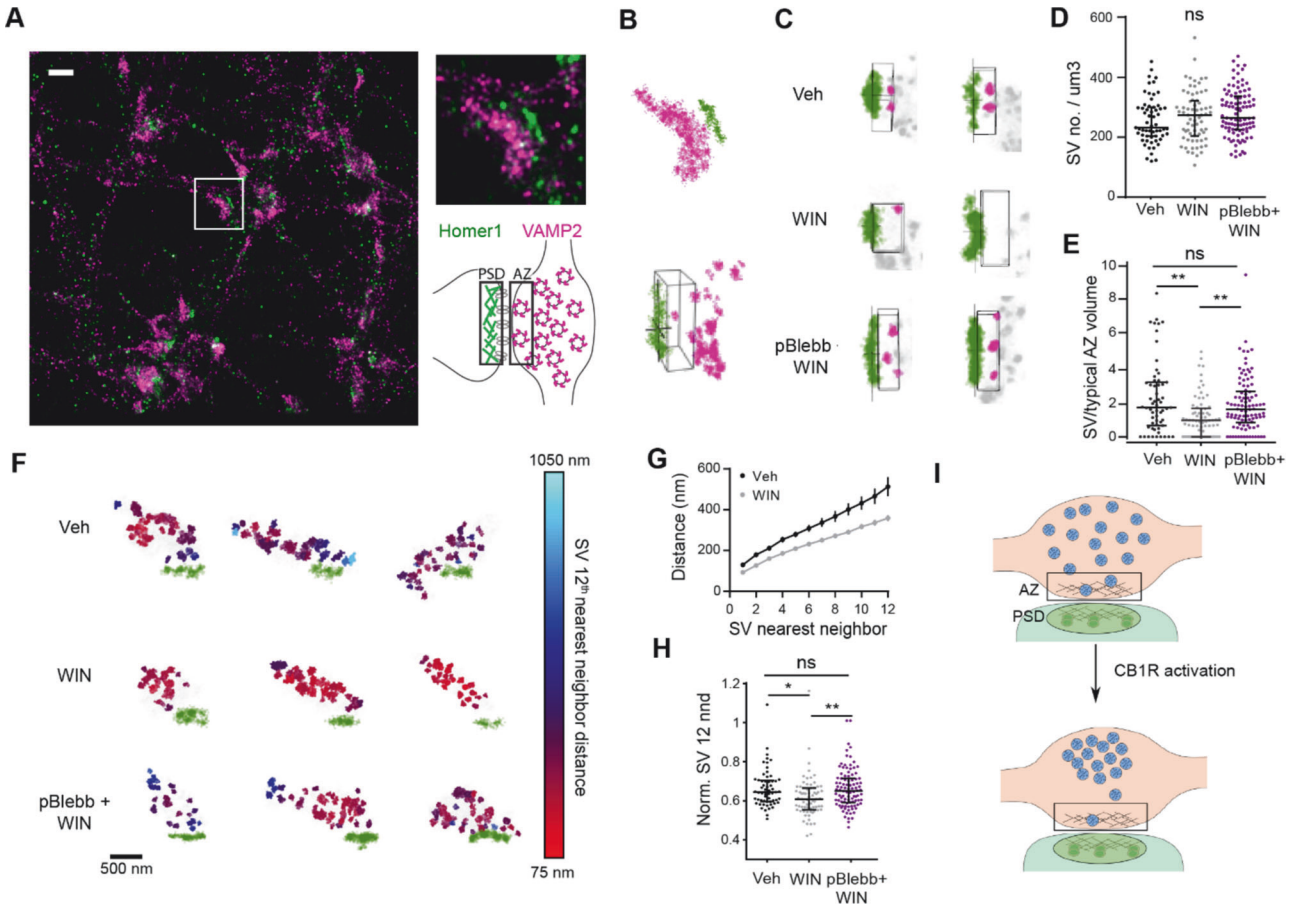

Fig. 3 STORM imaging shows that actomyosin contractility is necessary for CB_1R-induced redistribution of synaptic vesicles within the presynaptic bouton. A STORM reconstruction of cultured hippocampal neurons stained against VAMP2 (magenta) and Homer1 (green). **B** DBSCAN clustering results for VAMP2 and Homer1 synaptic appositions of the synapse shown in (**A**). Left: side view of the synapse showing presynaptic clustering of VAMP2 and postsynaptic clustering of Homer1. Right: 3D angled view of the synapse showing the estimated AZ volume and the synaptic vesicles identified from VAMP2 localizations. **C** Representative examples of SVs contained within the estimated active zone (AZ) volume under Vehicle and WIN treatment conditions. Vesicles contained within the volume are in magenta, those outside are in dark gray, Homer1 postsynaptic apposition is in green. **D** Normalized number of identified synaptic vesicles (SVs) per synapse for each condition tested. Neither WIN nor pBlebb significantly affect the total number of SVs located within boutons (Veh: $n = 59$, 255 ± 10 SVs; WIN: $n = 70$, 269 ± 10 SVs; pBlebb: $n = 98$, 280 ± 8 SVs; $p = 0.119$ Kruskal–Wallis test with Dunn's multiple comparisons correction) **E** Normalized number of SVs identified within the estimated AZ volume per synapse over different treatment conditions. Numbers were normalized to the mean AZ volume estimated over all synapses (Fig. 2F). Inhibition of actomyosin contraction with pBlebb prevents the reduction in SVs contained within the AZ volume measured under CB_1R activation (Veh: $n = 59$, 2.24 ± 0.27 SVs; WIN: $n = 70$, 1.16 ± 0.14 SVs; pBlebb: $n = 98$, 1.87 ± 0.16 SVs; $p = 0.0008$ Kruskal–Wallis test with Dunn's multiple comparisons correction) **F** Representative examples of SV clustering within boutons per treatment condition. **G** Graph showing median distance of SVs to their nth nearest neighbor under Veh and WIN treatments. Error bars: SEM. **H** Normalized SV 12th nearest neighbor distances (nnd) per bouton for each treatment condition. pBlebb treatment significantly prevents the SV clustering observed under CB_1R activation (Veh: $n = 59$, 0.664 ± 0.013; WIN: $n = 70$, 0.617 ± 0.012; pBlebb: $n = 98$, 0.662 ± 0.01; $p = 0.0022$ Kruskal-Wallis test with Dunn's multiple comparisons correction) **I**. Schematic representing the observed redistribution of SV through actomyosin contraction under CB_1R activation.

when pretreating neurons with pBlebb (Fig. 3H). These results indicate that actomyosin contraction induced by CB_1R activation leads to a redistribution of SV within presynaptic boutons that may prevent accessibility of vesicles to the active zone (Fig. 3I).

NMII and ROCK activation are necessary for the full inhibition of the readily releasable pool of vesicles (RRP) induced by CB_1R. Our STORM assay shows that CB_1R activation leads to a reduction in the number of SVs proximal to the AZ. This reduction could suggest a reduction of the RRP, which would explain the inhibition of synaptic activity typically associated with CB_1R activation. While we have shown that SV cycling is decreased after CB_1R activation when neurons are depolarized with high potassium in our paradigm, the strong stimulation likely recruits several pools of vesicles, including both the RRP and the recycling pool. We therefore modified our sypH2 assay to specifically measure the turnover of the RRP by repeated and rapid electrical stimulation of synapses.

Firstly, we increased acquisition frequency to be able to image separate release events, allowing us to compare SV turnover before and after application of inhibitors within single synapses, giving us more precise and reliable measurements. Secondly, instead of KCl, release was evoked through field stimulation of the transfected neurons using trains of 20–40 stimulations at 20 Hz to limit release to the RRP [43]. Stimulation of cultures in this manner yielded reliably stable release events (Fig. 4A–C; Supplementary Fig. 1). As fewer stimulations evoked smaller fluorescence peaks in the same boutons (Supplementary Fig. 1), these release events most likely result from the release of a steady RRP.

With this method, a strong reduction of release was observed as early as 30 s after bath application of WIN (1 μM), and persisted over

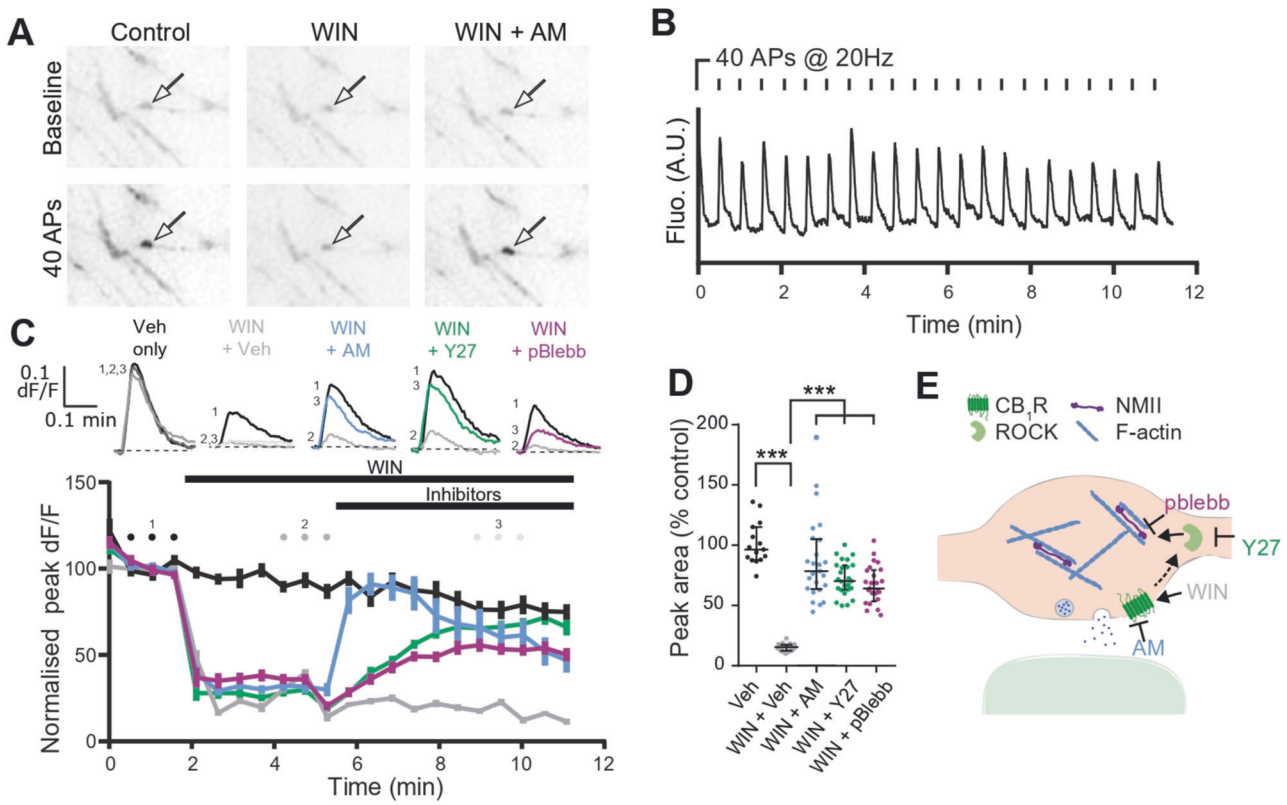

Fig. 4 Actomyosin contractility through ROCK is necessary for CB_1R-induced inhibition of the SV readily releasable pool (RRP). **A** Representative image of an axonal bouton transfected with sypH2 at baseline (top) and during 20 Hz train stimulations (40 APs - bottom) under different treatment conditions **B** Representative trace of bouton fluorescence responses in control conditions throughout the stimulation paradigm. Neurons were stimulated every 30 s with trains of 40 stims (APs) at 20 Hz **C** Top: Representative traces of 3 averaged normalized fluorescence responses to stimulation per treatment condition (time points correspond to the circles over the traces on the bottom): 1. no treatment (control - black), 2. treatment (dark gray), and 3. post-treatment (light gray). Bottom: Average normalized peak fluorescence intensities per stimulation train over time in each treatment condition. **D** Fluorescence peak areas as a percentage of control for all boutons tested. AM251 (AM), para-nitroblebbistatin (pBlebb), and Y-27632 (Y27) all significantly recovered vesicle release from inhibition by WIN (WIN: 15.12 ± 0.6, n = 25; Vehicle: 101.1 ± 4.56, n = 15, vs WIN: $p < 0.0001$; AM + WIN: 86.85 ± 6.6, n = 25, vs WIN: $p < 0.0001$; pBlebb + WIN: 64.27 ± 3.13, n = 25, vs WIN: $p < 0.0001$; Y27 + WIN: 69.72 ± 2.72, n = 25, vs WIN: $p < 0.0001$; Kruskal–Wallis test with Dunn's correction for multiple comparisons) indicating that WIN inhibition is both CB_1R dependent and dependent on actomyosin contraction through ROCK. **E** Schematic showing the molecular pathway tested linking CB_1R activation to actomyosin contraction during synaptic vesicle release at an axonal bouton. SypH2: synaptophysin-pHluorin; Veh: Vehicle; WIN: WIN55,212-2; AM: AM251; pblebb: para-nitroblebbistatin; Y27: Y-27632.

the duration of the experiment (10 min) (Fig. 4C; Supplementary Fig. 2). Application of the agonist with the CB_1R inverse agonist AM251 (AM - 10uM) significantly recovered release from inhibition, indicating that the inhibition of the RRP under WIN application was specific to CB_1R activation (Fig. 4; Supplementary Fig. 2).

Applied alone, pBlebb (2 µM) caused a mild inhibition in release: a difference in median of 8% in comparison to a Vehicle control (Supplementary Fig. 3). Nonetheless, both pBlebb and Y27 (10 µM) substantially reversed CB_1R-induced inhibition when applied with the CB_1R agonist (Fig. 4C–E; Supplementary Fig. 2), indicating that contractility of the actomyosin cytoskeleton is at least partly necessary for inhibition of the RRP under CB_1R.

As both NMII and ROCK inhibition produce a substantial reversal of the effects of direct activation of CB_1R on the RRP, these results extend our observations with STORM, suggesting that, just as actomyosin contractility is necessary for the physical redistributions of vesicles away from the AZ under CB_1R activation, it is also responsible for inhibiting the release of the RRP after CB_1R activation.

Actomyosin contractility is necessary for CB_1R-induced LTD at glutamatergic cortico-striatal synapses. We have so far shown in neuronal cultures that actomyosin recruitment under CB_1R activation occludes SV release and induces a redistribution of SV within pre-synaptic boutons at glutamatergic synapses. One of the main physiological roles of CB_1R in the CNS is in the mediation of both short- and long-term forms of synaptic plasticity. This plasticity is accomplished through the post-synaptic production and release of endocannabinoids (eCB), the endogenous agonists of CB_1R. While short-term CB_1R plasticity has been established to occur through the inhibition of presynaptic voltage-gated calcium channels (VGCC) and activation of inwardly rectifying potassium channels, likely through the recruitment of the β/γ G-protein subunits under CB_1R activation (reviewed in [3]), the long-term effects are comparatively less understood. We therefore tested whether recruitment of actomyosin contractility under CB_1R could play a role in CB_1R-induced LTD.

The induction of CB_1R-dependant forms of plasticity are known to be sensitive to both the molecular environment and activity history of the synapse [44], conditions which may differ at different synapse types [45] and which, to our knowledge, have not yet been described in cell culture models. We therefore chose to test our hypothesis in a known model of CB1R LTD, the glutamatergic cortico-striatal synapse at medium-sized spiny neurons (MSNs) of the dorsolateral striatum (Fig. 5A). MSNs express eCB-mediated and CB_1R-dependent STD, namely a

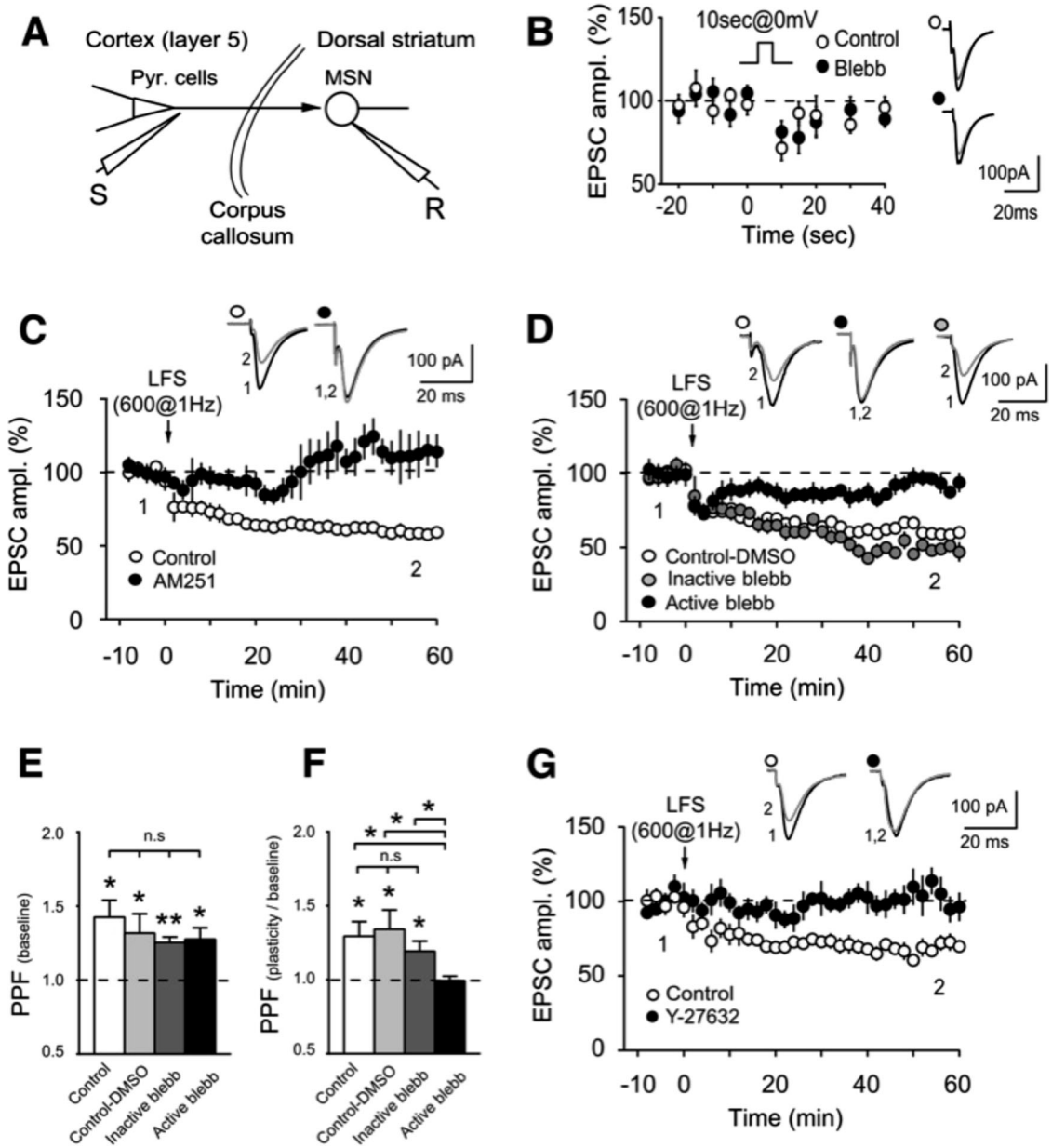

Fig. 5 Pre-synaptic actomyosin contractility mediates eCB-LTD at excitatory cortico-striatal synapses. A Schematic of a whole-cell recording of a MSN in the dorsal striatum with stimulation in the somatosensory cortical layer V. (MSN: medium-sized spiny neurons). **B** The eCB induced DSE following a 10 s depolarization at 0 mV (white circles, 81 ± 4% of baseline, n = 13, p = 0.0003) was unaffected by blebbistatin (black circles, 79 ± 3% of baseline, n = 11, p = 0.0001 with baseline; p = 0.8039 with control DSE, n = 13). Average sample traces before and 10 s after the depolarization are shown on the right. **C** The selective CB1R antagonist AM251 inhibited LTD induced with LFS (control: 58 ± 2% of baseline, n = 7, p < 0.0001 with baseline; AM251: 107 ± 10% of baseline, n = 5, p = 0.5244 with baseline, p < 0.0001 with control), indicating the LTD was eCB-mediated. **D** The eCB-LTD following a LFS (white circles, control-DMSO: 56 ± 7% of baseline, n = 9, p = 0.0002, p = 0.8217 with control without DMSO) was abolished in the presence of blebbistatin (black circles, 95 ± 3% of baseline, n = 10, p = 0.1201 with baseline, p < 0.0001 with control LTD) but was unaffected by the inactive enantiomer of blebbistatin (gray circles, 10 μM, 52 ± 4% of baseline, n = 11, p < 0.0001 with baseline, p = 0.0556 with control LTD). Average sample traces are shown on top at the time point before (1) and after the stimulation protocol (2). **E** 50 ms inter-stimuli intervals induced significant paired-pulse facilitation (PPF) in control (p = 0.0203, n = 5), control-DMSO (p = 0.0120, n = 8), inactive blebbistatin (p = 0.0023, n = 5) and active blebbistatin (p = 0.0375, n = 4) conditions (ANOVA: p = 0.6291 and F(3, 18) = 0.5905). **F** PPF plasticity/baseline displayed significant increase in control (PPF plasticity/baseline = 1.30 ± 0.10, p = 0.0397, n = 5), control-DMSO (PPF plasticity/baseline = 1.34 ± 0.13, p = 0.0335, n = 8) and inactive blebbistatin (PPF plasticity/baseline=1.19 ± 0.07, p = 0.0493, n = 5; ANOVA: p = 0.6630 and F(2, 15) = 0.4225) but not for active blebbistatin (PPF plasticity/baseline=1.00 ± 0.03, p = 0.8697, n = 4). **G** The ROCK inhibitor Y-27632 abolishes eCB-LTD (black circles, 98 ± 11% of baseline, n = 7, p = 0.7204 with baseline, p = 0.0038 with control LTD, n = 6). Average sample traces are shown on top for time points (1) and (2). Student's t-test. Values: mean ± SEM.

depolarization-induced suppression of excitation (DSE), and LTD [46, 47]. Here, a sustained depolarization of MSNs induced a DSE (Fig. 5B), which was not significantly affected by blebbistatin (10 μM) treatment (Fig. 5B), indicating actomyosin contraction is not implicated in the short-term plasticity induced by CB_1R.

We then tested the striatal eCB-LTD induced after cortical low frequency stimulation (LFS) [47, 48]. This LTD was indeed CB_1R-mediated as it was prevented by treatment with the CB_1R

specific inhibitor AM251 (3 μM) (Fig. 5C). Actomyosin contraction was found to be necessary for corticostriatal eCB-LTD, which was prevented by treatment with blebbistatin, but not with the inactive blebbistatin enantiomer (Fig. 5D). This effect was not due to alterations in basal transmission as we found no significant change in PPR for 50 ms intervals inter-stimuli in any tested condition (Fig. 5E).

We further evaluated whether the effect of blebbistatin on eCB-LTD was pre- or post-synaptic by measuring the paired-pulse facilitation (PPF) ratio before and after LFS ($PPF_{plasticity/baseline}$). We found a significant increase in PPF in control conditions, whereas no significant variation of PPF was found following treatment with active blebbistatin (Fig. 5F), indicating a pre-synaptic action of actomyosin contraction under eCB-LTD. The specific ROCK inhibitor Y-27632 (10 μM) also impaired eCB-LTD induction (Fig. 5G). Therefore, activation of CB_1R by eCBs in cortico-striatal glutamatergic synapses induces LTD, but not short-term depression, through ROCK-mediated presynaptic actomyosin contraction.

DISCUSSION

In this study, we show that CB_1R activation inhibits the release of the presynaptic RRP in cultured neurons through ROCK activation and actomyosin contractility. Through STORM super-resolution imaging, we show that actomyosin recruitment induces a spatial reorganization of excitatory presynaptic vesicle pools under CB_1R activation, providing a mechanistic explanation for the inhibitory effects of CB_1R on SV release. We further show that actomyosin recruitment is necessary for CB_1R-LTD at glutamatergic synapses in the striatum, while leaving short-term plasticity unaffected. Taken together, these results suggest a novel model explaining CB_1R-induced long-term plasticity, whereby recruitment of the actomyosin cytoskeleton induces clustering of SV pools, hindering access of vesicles to the AZ for release, thereby inhibiting synaptic transmission. Our results significantly extend the suggested roles for the pre-synaptic actin cytoskeleton (Rust & Maritzen, 2015), advancing toward a more complete model of regulation of SV release.

CB_1R-induced recruitment of actomyosin and SV release

Here, we show the direct involvement of both NMII and ROCK in the modulation of synaptic neurotransmission by CB_1R. Specific recruitment of NMII through CB_1R has previously been found to be necessary for the chemorepulsive effects of cannabinoids during axonal pathfinding in development [13, 14]. However, recruitment of this pathway in synapses had not yet been studied. By using a sypH2 assay, we show that ROCK and NMII can specifically be recruited pre-synaptically to enact the inhibition of SV release induced by CB_1R.

CB_1R has been shown to interact with the actin cytoskeleton at mature neurons. Indeed, a proteomic study has shown that CB_1R can interact with WAVE1, an F-actin modulating protein complex, at mature neurons [49] and Monday et al. [15]. show that the synthesis of WAVE1 and its downstream effector Arp2/3 is decreased upon CB_1R activation. However, the pre-synaptic locus of this modulation is unclear, as it was found that CB_1R modulation of WAVE1 may induce decreases in dendritic spine volumes [49]. Monday et al. [15]. further show that the activation of Rac1, an important promoter of actin polymerization, is critical in CB_1R-LTD, and its inhibition induces a concomitant decrease in PPR, suggesting that the recruitment of Rac1 under CB_1R is presynaptic and directly affects synaptic vesicle release. They also find that stabilization of the actin cytoskeleton with jasplakinolide precludes CB_1R-LTD. Taken together with the present study, these results provide strong evidence for the importance of actomyosin dynamics in the inhibition of release induced by CB_1R.

CB_1R, actomyosin and the SV pool

We show through STORM microscopy that CB_1R activation can induce a redistribution of SV within presynaptic terminals, and that actomyosin contractility is necessary for these effects. Several electron microscopy studies have previously shown a redistribution of vesicle pools under CB_1R activation and CB_1R knock-out at various synapses [7–11]. Our results here further extend these findings by bringing forth actomyosin contractility as a key mechanistic driver in CB_1R-induced synaptic vesicle redistribution. Notably, a recent study has shown that CB_1R activation increases SV pool clustering within presynaptic terminals [10], similarly to our results. Interestingly, they suggest this clustering may result from the activation of synapsin, as they find that CB_1R activation increases the dephosphorylated state of synapsin at presynaptic terminals. Structurally, dephosphorylated synapsin reversibly tethers SV [38, 39], particularly vesicles of the recycling and/or resting pool [50], to the actomyosin cytoskeleton. Increasing SV tethering to the actin cytoskeleton through synapsin may further amplify the clustering effect of actomyosin contraction we find in the present study. Future studies should clarify the extent to which synapsin recruitment and actomyosin contractility may contribute synergistically to the effects of CB_1R activation.

Results from previous studies support a role for actomyosin dynamics in the regulation of synaptic vesicle pool distribution. Firstly, actin filaments are located to restrict vesicle movement as they are found intertwined within presynaptic vesicle pools [38, 39], where they can reversibly bind to vesicles through synapsin [38, 39]. Furthermore, alteration of actomyosin dynamics, either through F-actin stabilization [23] or through MLCK inhibition [7] leads to a redistribution of SV away from the active zone. Importantly, a recent superresolved microscopy study reported, in addition to intertwined filaments, actin corrals around SV pools [24]. Together, these findings suggest a 'barrier' role of the actomyosin cytoskeleton, whereby actin filaments can restrict SV movement within and out of recovery pools to modulate replenishment of the RRP. Our results confirm this model as we find that activation of actomyosin contraction through CB_1R induces a clustering of SV within presynaptic terminals and a depletion of vesicles from the AZ.

Actomyosin and CB_1R-induced short- and long-term depression

By showing that both NMII and ROCK are necessary for CB_1R-LTD at glutamatergic synapses, our findings provide a novel mechanism explaining CB_1R-LTD. Taken together, our results suggest a mechanism whereby actomyosin contractility causes a clustering of SV within the presynaptic compartment and away from the AZ, precluding SV long-term release. Notably, we did not observe an effect of either NMII or ROCK inhibition on DSE, the short-term form of CB_1R-induced synaptic plasticity at glutamatergic synapses. CB_1R has been shown to inhibit SV release through inhibition of N-type voltage-gated calcium channels and activation of GIRK channels via $G_{\beta/\gamma}$ subunits [51, 52]. This pathway is mostly thought to be implicated in short-term plasticity. Our results confirm this since both NMII and ROCK inhibitors substantially reversed the inhibition of SV release seen with CB_1R activation, both in culture and in brain slices, while not having comparable effects on transmission applied on their own. This implies that NMII and ROCK inhibitors do not have a substantial effect on calcium channel activity and therefore, that the reversal effect of NMII and ROCK inhibition directly pertains to affecting actomyosin contractility. Furthermore, CB_1R-STD occurs very rapidly (<1 s), following brief activation of CB_1Rs while a longer CB_1R activation (>5 min) is necessary for CB_1R-LTD induction [45]. This longer activation period may be needed to engage actomyosin contraction which was found to occur over several minutes in non-muscular cells [53].

CB_1R-induced presynaptic activation of actomyosin contractility

How does CB_1R activation lead to the activation of the actomyosin cytoskeleton? In the present study, we show that the activation of ROCK, an upstream regulator of myosin contractility, is necessary for the inhibition of SV release and CB_1R-LTD, suggesting the recruitment of a specific molecular pathway linking CB_1R to NMII. We have previously shown that axonal growth cone collapse under CB_1R activation is dependent on the activation of RhoA, ROCK and NMII, and preventing the expression of $G_{12/13}$ proteins with small interfering RNA prevented these effects [14]. This study therefore provided a full molecular pathway linking CB_1R activation to actomyosin contraction in axonal growth cones through the recruitment of $G\alpha_{12/13}$ subunits. Although here we do not explore the full molecular pathway, the effects of ROCK inhibition in the present study suggest a similar pathway could be at play in the presynaptic terminal. Our results however do not preclude the involvement of other G-protein α subunits under CB_1R activation. Previous studies have noted the involvement of the $G_{i/o}$ /cAMP/PKA molecular pathway in the effects of CB_1R on SV pool distribution and release [8, 9] and CB_1R-LTD [54, 55]. Inhibition of PKA through $G_{i/o}$ also best explains the dephosphorylation of synapsin seen under CB_1R activation [10]. While the RhoA-mediated activation of ROCK has typically been associated to the activation of $G_{12/13}$ [56], there is evidence in non-neuronal cells that PKA can inhibit RhoA/ROCK activity [57–59]. There is a possibility, therefore, that the activation of ROCK and NMII that we observe under CB_1R activation in our study may be induced by $G_{i/o}$.

Another possibility combining these two theories is the parallel recruitment of both $G_{12/13}$ and $G_{i/o}$ during prolonged activation of CB_1R. As mentioned above, CB_1R-LTD induction requires the prolonged activation of CB_1R over several minutes [45]. While CB_1R has been found to preferentially associate to G_i subunits in neuroblastoma cells [60], it is also capable of coupling to other Gα subunits [14, 61–63]. Notably, it was found that exacerbating $G_{i/o}$ availability could induce the recruitment of other Gα subunits by CB_1R [61]. It is possible therefore that the prolonged activation of CB_1R necessary for LTD increases the probability of $G_{12/13}$ recruitment concomitant to $G_{i/o}$. Further investigations using targeted pharmacological and genetic modulation of G-protein subunits specifically in the presynaptic terminals are needed to establish their respective role in the mediation of CB_1R effects.

In conclusion, our findings identify a major actin binding/structuring protein, the contractile NMII, mechanistically explaining, through the dynamic redistribution of SV, the generation of cannabinoid-induced long-term presynaptic plasticity. Our results, by reporting a conceptually novel molecular mechanism of synaptic plasticity downstream of CB_1R, an important target of both endocannabinoids and marijuana, a known risk factor in schizophrenia [64], open novel perspectives in the understanding of cognitive function and neuro-psychiatric disease.

MATERIALS AND METHODS

Animals

Experiments were performed in accordance with local animal welfare committee (Center for Interdisciplinary Research in Biology and EU guidelines; directive 2010/63/EU). Rats and mice (Charles River, L'Arbresle, France) were housed in standard 12 h light/dark cycles and food and water were available ad libitum.

Antibodies and Chemicals

Rabbit polyclonal Homer1 (Cat. No. 160 003) and mouse monoclonal VAMP2 (Cat. No. 104 211) antibodies were obtained from Synaptic Systems (Goettingen, Germany). Bassoon mouse monoclonal antibody (Cat. No. ab82958) was obtained from Abcam (Paris, France). Paired fluorophore-conjugated secondary antibodies were made as previously described [65]. WIN 55212-2 and (RS)-3,5-DHPG were from Tocris. Carbachol, Y-27632, active (S)-(−)-blebbistatin and inactive (R)-(+)-blebbistatin enantiomers and para-Nitroblebbistatin were from Calbiochem, Sigma and Optopharma. None of the bath-applied drugs had a significant effect on basal IPSC and EPSC amplitudes, in our experimental conditions.

Primary cultures of hippocampal neurons and transfections

Dissociated neurons obtained from hippocampi of day 17–18 Sprague-Dawley rat embryos were plated on Poly-D-Lysine-coated coverslips at a density of approximately 100,000 cells per coverslip (18 mm) and subsequently cultivated at 37 °C, 5% CO_2 in Neurobasal™ (LifeTech) medium supplemented with 2% B27 (LifeTech), 0.5 mM L-glutamine, 10 U/mL penicillin G and 10 mg/mL streptomycin containing conditioned medium, obtained by incubation with cortical glial cultures (from 4 days old rat pups, 70-80% confluence) for 24 h as described previously [14]. Neurons were transfected at 6–7 DIV, either with synaptophysin-pHluorin 2x (sypH2) [26], a kind gift from Dr. Stefan Krueger (Dalhousie University, Halifax, NS, Canada), and LifeAct-mCherry, kind gift of G. Montagnac and P. Chavrier (Institut Curie, Paris, France), or with sypH2 alone, by using the Lipofectamine 2000™ method (Life Tech).

Time-lapse microscopy of primary cultured neurons with chemical stimulation

For the experiments of Fig. 1, transfections and imaging were performed as previously described [14], with a couple of exceptions. Time-lapse microscopy was performed between DIV 16 to 19 and images were acquired every minute. Neurons were depolarized by 50 mM KCl for 2 min, followed by 50 mM NH4Cl treatment. Pretreatments and treatments were applied at 30 min and 10 min before KCl, respectively, after acquisition of a 10 min baseline without treatment for normalization. Dimethylsulfoxide vehicle concentrations ranged from 0.02% to 0.1%. Image stacks were realigned using ImageJ. SypH2 fluorescence intensity was measured in round ROIs of approximately 3 × 3 µm, placed manually around visually identified axonal boutons, with mean basal axonal fluorescence intensity subtracted for each timepoint. Axonal boutons were selected for analysis if SpH response to NH4Cl was superior to that of KCL and if baseline fluorescence was within 2× the standard deviation around baseline population mean. Typical statistical analyses used Kruskal-Wallis test with Dunn's post-hoc Multiple Comparison Test, n indicates the number of axonal boutons analyzed. Values are mean ± SEM.

Time-lapse microscopy of primary cultured neurons with electrical stimulation

For the measuring RRP, time-lapse microscopy and quantifications of synaptic function were performed by electrical field stimulations of hippocampal neurons according to an adapted method using sypH2 fluorescence changes [43]. We used a custom modified Warner RC-49MFSH perfusion chamber equipped with several injection canulas, and two platinum wires passing through the seal gasket holding the 18 mm coverslip (to maintain a fixed geometry of the chamber). To maximize the number of synapses stimulated in a single field, we used a Nikon DS-Qi2 wide field camera driven by the NIS 4.30.01 software on a Nikon i2 Eclipse microscope (60 × objective) equipped with a 37 °C chamber. Neurons were monitored in a video buffer containing 136 mM NaCl, 2.5 mM KCl, 2 mM $CaCl_2$, 1.3 mM $MgCl_2$, 10 mM D-glucose and 10 mM Hepes, at pH 7.4. To avoid indirect stimulations of the neurons and establish the synchronicity of synaptic responses with electrical stimulations, the postsynaptic component was inhibited by the NMDA receptor antagonist AP5 (50 µM) and the AMPA receptor antagonist CNQX (25 µM) in all solutions. Electrical field stimulations with controlled parameters were provided by a Grass S48 stimulator (Grass Instruments, Quincy, MA). Experiments were usually performed between 17 and 25 DIV (11–19 days post transfection) when enough synapses were mature to ensure robust sypH2 signals. A constant concentration of 0.1% BSA and 0.3% Dimethysulfoxide (vehicle) was maintained during all experiments. Stimulations were typically performed with the following parameters: the quantitative release of the Readily Releasable Pool (RRP) of synaptic vesicles was obtained with a train of 40 Action Potentials (APs) of 1 ms at 20 Hz with a voltage of 100 V. The complete recovery of the RRP was usually obtained after a time lapse of 30 s. The quantitative release of the Recycling Pool (RP) was obtained with a train of 900–1000 APs of 1 ms at 20 Hz (100 V) with a recovery time of several minutes.

Videos of axons were performed with a time-lapse of 300 ms. A single field (200 × 200 µm) usually contained several tens to several hundreds of responding synapses. Image stacks were analyzed using ImageJ software [66]. SypH2 fluorescence intensity was measured in round ROIs of

approximately 3–4 µm, placed manually around visually identified axonal boutons. Fluorescence profiles for each synapse were plotted and peak areas were used for the quantification of synaptic response to electrical stimulations. Unless otherwise noted, statistical analyses were performed using a Kruskal-Wallis test with Dunn's post-hoc multiple comparisons correction, n indicates the number of axonal boutons analyzed, and values indicated mean ± SEM.

Immunocytochemistry and STORM imaging

Cultured neurons between 18–22 DIV were pretreated with either a DMSO Vehicle (0.001%) or with para-nitroblebbistatin (25 µM) in videomicroscopy medium for 20 min. Either WIN (1 µM) or a DMSO Vehicle (0.0001%) was subsequently added to the wells for 10 min. Neurons were then immediately fixed with a preheated solution of 4% PFA and 4% sucrose in 0.1 M phosphate buffered saline (PBS) for 15 min at room temperature (RT), permeabilized after wash for 5 min at RT with 0.1% Triton X in PBS, and blocked for 1 h at RT with blocking buffer (4% BSA in PBS). Primary and secondary antibodies were applied in blocking buffer, primary antibodies being applied overnight at 4 °C and secondary antibodies being applied subsequently, after a PBS wash, for 2 h at RT. After washing out the secondary antibody, neurons were post-fixed with 4% PFA and 4% sucrose in PBS for 5 min, washed and stored in PBS at 4 °C before imaging.

STORM images were acquired on a N-STORM microscope (Nikon Instruments), outfitted with 405 nm, 561 nm, and 647 nm solid-state lasers, a 100X NA 1.49 objective and an Ixon DU-897 camera. Imaging was performed as previously described [65]. Briefly, visually identified dendrites labeled with activator-reporter fluorophore pairs (Alexa Fluor 405 - Alexa Fluor 647 and Cy3 - Alexa Fluor 647) were imaged using sequences of one activator frame (405 or 561 nm) followed by three reporter frames (647 nm) [34]. A cylindrical lens was placed across the optical path in order to acquire 3D information [67].

STORM image processing

STORM localizations were identified using the ThunderStorm plugin [68] in ImageJ software [66]. Images were filtered with a B-spline wavelet filter of order 3 and scale 2. Approximate localization of molecules was performed by local maximum within an 8-connected neighborhood after thresholding at 2.5 * the standard deviation of the first wavelet level of the wavelet filter [69]. Sub-pixel localization of molecules was then performed by Maximum likelihood fitting with an elliptical Gaussian. Subsequently, activator-reporter allocation and drift correction were performed using custom ImageJ macros and R scripts.

Electrophysiological recordings and analysis from corticostriatal slices

330 µm horizontal brain slices containing the somatosensory cortex and the corresponding corticostriatal projection field in the dorsolateral striatum were prepared from P25-35 male rats as previously described [48]. Brains were sliced in a 95% CO_2/5% O_2-bubbled, ice-cold cutting solution containing (in mM) 125 NaCl, 2.5 KCl, 25 glucose, 25 $NaHCO_3$, 1.25 NaH_2PO_4, 2 $CaCl_2$, 1 $MgCl_2$, 1 pyruvic acid, and then transferred into the same solution at 34 °C for one hour and then moved to room temperature before patch-clamp whole-cell recordings (at 34 °C).

Patch-clamp recordings were performed as previously described [48]. Briefly, borosilicate glass pipettes of 4–6 MOhms resistance contained for whole-cell recordings (in mM): 105 K-gluconate, 30 KCl, 10 HEPES, 10 phosphocreatine, 4 ATP-Mg, 0.3 GTP-Na, 0.3 EGTA (adjusted to pH 7.35 with KOH). The composition of the extracellular solution was (mM): 125 NaCl, 2.5 KCl, 25 glucose, 25 $NaHCO_3$, 1.25 NaH_2PO_4, 2 $CaCl_2$, 1 $MgCl_2$, 10 mM pyruvic acid bubbled with 95% O_2 and 5% CO_2. Signals were amplified using EPC10-2 amplifier (HEKA Elektronik, Lambrecht, Germany). All recordings were performed at 34 °C and slices were continuously superfused at 2–3 ml/min with the extracellular solution. Slices were visualized on an Olympus BX51WI microscope (Olympus, Rungis, France) using a 4×/0.13 objective for the placement of the stimulating electrode and a 40×/0.80 water-immersion objective for localizing cells for whole-cell recordings. Series resistance was not compensated. Current-clamp recordings were filtered at 2.5 kHz and sampled at 5 kHz and voltage-clamp recordings were filtered at 5 kHz and sampled at 10 kHz using the Patchmaster v2x32 program (HEKA Elektronik). Electrical stimulations were performed with a bipolar electrode (Phymep) placed in the layer 5 of the somatosensory cortex and were monophasic at constant current (ISO-Flex stimulator) [47, 48]. Currents were adjusted to evoke striatal EPSCs ranging in amplitude from 50 to 200 pA. Repetitive control stimuli were applied at a frequency of 0.1 Hz for 60 min after LFS protocol. Recordings on neurons were made over a period of 10 min at baseline, and for at least 60 min after the LFS protocols; long-term changes in synaptic efficacy were measured from 45 to 55 min. We individually measured and averaged 60 successive EPSCs, comparing the last 10 min of the recording with the 10-min baseline recording. Series resistance was monitored for each sweep and a variation above 20% led to the rejection of the experiment. LTD was induced with low frequency stimulation protocol consisting in 600 cortical stimulations at 1 Hz paired with postsynaptic concomitant depolarization of the MSN during 50 ms [47, 48]. For DSE induction, MSN was depolarized from RMP to 0 mV during 10 s (with bath-applied carbachol, 10 µM, and DHPG, 50 µM) [47, 48]. Off-line analysis was performed using Fitmaster (Heka Elektronik) and Igor-Pro 6.0.3 (Wavemetrics, Lake Oswego, OR, USA). Statistical analysis was performed using Prism 5.0 software (San Diego, CA, USA). "n" refers to a single cell experiment from a single slice Bleckert et al. [70]; Mochida et al. [71].

DATA AVAILABILITY

The data that support the findings of this study are available from the senior authors, LV and ZL, upon reasonable request.

CODE AVAILABILITY

All R scripts used for the STORM analysis are available on github at https://github.com/mahmcfadd/mcfadd-storm.git.

REFERENCES

1. Cristino L, Bisogno T, Di Marzo V. Cannabinoids and the expanded endocannabinoid system in neurological disorders. Nat Rev Neurol. 2020;16:Article 1. https://doi.org/10.1038/s41582-019-0284-z.
2. Lutz B, Marsicano G, Maldonado R, Hillard CJ. The endocannabinoid system in guarding against fear, anxiety and stress. Nat Rev Neurosci. 2015;16:705–18. https://doi.org/10.1038/nrn4036.
3. Castillo PE, Younts TJ, Chávez AE, Hashimotodani Y. Endocannabinoid signaling and synaptic function. Neuron. 2012;76:70–81. https://doi.org/10.1016/j.neuron.2012.09.020.
4. Herkenham, Lynn M, Little AB, Johnson MD, Melvin MR, Costa LS, et al. Cannabinoid receptor localization in brain. Proc Natl Acad Sci USA. 1990;87:1932 https://doi.org/10.1073/pnas.87.5.1932.
5. Matsuda LA, Bonner TI, Lolait SJ. Localization of cannabinoid receptor mRNA in rat brain. J Comp Neurol. 1993;327:535–50. https://doi.org/10.1002/cne.903270406.
6. Zhang Y, Chen K, Sloan SA, Bennett ML, Scholze AR, O'Keeffe S, et al. An RNA-sequencing transcriptome and splicing database of glia, neurons, and vascular cells of the cerebral cortex. J Neurosci. 2014;34:11929–47. https://doi.org/10.1523/JNEUROSCI.1860-14.2014.
7. García-Morales V, Montero F, Moreno-López B. Cannabinoid agonists rearrange synaptic vesicles at excitatory synapses and depress motoneuron activity in vivo. Neuropharmacology. 2015;92:69–79. https://doi.org/10.1016/j.neuropharm.2014.12.036.
8. Alonso B, Bartolomé-Martín D, Ferrero JJ, Ramírez-Franco J, Torres M, Sánchez-Prieto J. CB1 receptors down-regulate a cAMP/Epac2/PLC pathway to silence the nerve terminals of cerebellar granule cells. J Neurochem. 2017;142:350–64. https://doi.org/10.1111/jnc.14059.
9. Ramírez-Franco J, Bartolomé-Martín D, Alonso B, Torres M, Sánchez-Prieto J. Cannabinoid type 1 receptors transiently silence glutamatergic nerve terminals of cultured cerebellar granule cells. PLoS ONE. 2014;9:e88594. https://doi.org/10.1371/journal.pone.0088594.
10. Patzke C, Dai J, Brockmann MM, Sun Z, Fenske P, Rosenmund C, et al. Cannabinoid receptor activation acutely increases synaptic vesicle numbers by activating synapsins in human synapses. Mol Psychiatry. 2021:1–16. https://doi.org/10.1038/s41380-021-01095-0.
11. Buceta I, Elezgarai I, Rico-Barrio I, Gerrikagoitia I, Puente N, Grandes P. Deletion of the cannabinoid CB1 receptor impacts on the ultrastructure of the cerebellar parallel fiber-Purkinje cell synapses. J Comp Neurol. 2020;528:1041–52. https://doi.org/10.1002/cne.24808.
12. Ishii I, Chun J. Anandamide-induced neuroblastoma cell rounding via the CB1 cannabinoid receptors. NeuroReport. 2002;13:593–6.
13. Berghuis P, Rajnicek AM, Morozov YM, Ross RA, Mulder J, Urbán GM, et al. Hardwiring the brain: endocannabinoids shape neuronal connectivity. Science. 2007;316:1212–6. https://doi.org/10.1126/science.1137406.

14. Roland AB, Ricobaraza A, Carrel D, Jordan BM, Rico F, Simon A, et al. Cannabinoid-induced actomyosin contractility shapes neuronal morphology and growth. eLife. 2014;3:e03159. https://doi.org/10.7554/eLife.03159.
15. Monday HR, Bourdenx M, Jordan BA, Castillo PE. CB_1-receptor-mediated inhibitory LTD triggers presynaptic remodeling via protein synthesis and ubiquitination. eLife. 2020;9:e54812.
16. Cole JC, Villa BRS, Wilkinson RS. Disruption of actin impedes transmitter release in snake motor terminals. J Physiol. 2000;525:579–86. https://doi.org/10.1111/j.1469-7793.2000.t01-2-00579.x.
17. Kuromi H, Kidokoro Y. Two distinct pools of synaptic vesicles in single presynaptic boutons in a temperature-sensitive Drosophila mutant, shibire. Neuron. 1998;20:917–25. https://doi.org/10.1016/S0896-6273(00)80473-0.
18. Lee JS, Ho W-K, Lee S-H. Actin-dependent rapid recruitment of reluctant synaptic vesicles into a fast-releasing vesicle pool. Proc Natl Acad Sci USA. 2012;109:E765–74. https://doi.org/10.1073/pnas.1114072109.
19. Miki T, Malagon G, Pulido C, Llano I, Neher E, Marty A. Actin- and myosin-dependent vesicle loading of presynaptic docking sites prior to exocytosis. Neuron. 2016;91:808–23. https://doi.org/10.1016/j.neuron.2016.07.033.
20. Sakaba T, Neher E. Involvement of actin polymerization in vesicle recruitment at the calyx of held synapse. J Neurosci. 2003;23:837–46. https://doi.org/10.1523/JNEUROSCI.23-03-00837.2003.
21. Jordan R, Lemke EA, Klingauf J. Visualization of synaptic vesicle movement in intact synaptic boutons using fluorescence fluctuation spectroscopy. Biophys J. 2005;89:2091–102. https://doi.org/10.1529/biophysj.105.061663.
22. Shtrahman M, Yeung C, Nauen DW, Bi G, Wu X. Probing vesicle dynamics in single hippocampal synapses. Biophys J. 2005;89:3615–27. https://doi.org/10.1529/biophysj.105.059295.
23. Marra V, Burden JJ, Thorpe JR, Smith IT, Smith SL, Häusser M, et al. A preferentially segregated recycling vesicle pool of limited size supports neurotransmission in native central synapses. Neuron. 2012;76:579–89. https://doi.org/10.1016/j.neuron.2012.08.042.
24. Bingham D, Jakobs CE, Wernert F, Boroni-Rueda F, Jullien N, Schentarra E-M, et al. Presynapses contain distinct actin nanostructures. J Cell Biol. 2023;222:e202208110. https://doi.org/10.1083/jcb.202208110.
25. Bernstein BW, DeWit M, Bamburg JR. Actin disassembles reversibly during electrically induced recycling of synaptic vesicles in cultured neurons. Mol Brain Res. 1998;53:236–50. https://doi.org/10.1016/S0169-328X(97)00319-7.
26. Matz J, Gilyan A, Kolar A, McCarvill T, Krueger SR. Rapid structural alterations of the active zone lead to sustained changes in neurotransmitter release. Proc Natl Acad Sci USA. 2010;107:8836–41. https://doi.org/10.1073/pnas.0906087107.
27. Miesenböck G, De Angelis DA, Rothman JE. Visualizing secretion and synaptic transmission with pH-sensitive green fluorescent proteins. Nature. 1998;394:Article 6689. https://doi.org/10.1038/28190.
28. Kavalali ET, Jorgensen EM. Visualizing presynaptic function. Nat Neurosci. 2014;17:Article 1. https://doi.org/10.1038/nn.3578.
29. Ramírez-Franco J, Alonso B, Bartolomé-Martín D, Sánchez-Prieto J, Torres M. Studying synaptic efficiency by post-hoc immunolabelling. BMC Neurosci. 2013;14:127. https://doi.org/10.1186/1471-2202-14-127.
30. Denker A, Rizzoli S. Synaptic vesicle pools: an update. Front Synaptic Neurosci. 2010;2. https://www.frontiersin.org/articles/10.3389/fnsyn.2010.00135.
31. Kovács M, Tóth J, Hetényi C, Málnási-Csizmadia A, Sellers JR. Mechanism of blebbistatin inhibition of myosin II. J Biol Chem. 2004;279:35557–63. https://doi.org/10.1074/jbc.M405319200.
32. Vicente-Manzanares M, Ma X, Adelstein RS, Horwitz AR. Non-muscle myosin II takes centre stage in cell adhesion and migration. Nat Rev Mol Cell Biol. 2009;10:778–90. https://doi.org/10.1038/nrm2786.
33. Rizzoli SO. Synaptic vesicle recycling: steps and principles. EMBO J. 2014;33:788. https://doi.org/10.1002/embj.201386357.
34. Bates M, Huang B, Dempsey GT, Zhuang X. Multicolor super-resolution imaging with photo-switchable fluorescent probes. Science. 2007;317:1749–53. https://doi.org/10.1126/science.1146598.
35. Wilhelm BG, Mandad S, Truckenbrodt S, Krohnert K, Schafer C, Rammner B, et al. Composition of isolated synaptic boutons reveals the amounts of vesicle trafficking proteins. Science. 2014;344:1023–8. https://doi.org/10.1126/science.1252884.
36. Tang A-H, Chen H, Li TP, Metzbower SR, MacGillavry HD, Blanpied TA. A trans-synaptic nanocolumn aligns neurotransmitter release to receptors. Nature. 2016;536:210–4. https://doi.org/10.1038/nature19058.
37. Schikorski T, Stevens CF. Quantitative ultrastructural analysis of hippocampal excitatory synapses. J Neurosci. 1997;17:5858–67. https://doi.org/10.1523/JNEUROSCI.17-15-05858.1997.
38. Hirokawa N, Sobue K, Kanda K, Harada A, Yorifuji H. The cytoskeletal architecture of the presynaptic terminal and molecular structure of synapsin 1. J Cell Biol. 1989;108:111–26. https://doi.org/10.1083/jcb.108.1.111.
39. Landis DMD, Hall AK, Weinstein LA, Reese TS. The organization of cytoplasm at the presynaptic active zone of a central nervous system synapse. Neuron. 1988;1:201–9. https://doi.org/10.1016/0896-6273(88)90140-7.
40. Fornasiero EF, Raimondi A, Guarnieri FC, Orlando M, Fesce R, Benfenati F, et al. Synapsins contribute to the dynamic spatial organization of synaptic vesicles in an activity-dependent manner. J Neurosci. 2012;32:12214–27. https://doi.org/10.1523/JNEUROSCI.1554-12.2012.
41. Ryan TA, Li L, Chin LS, Greengard P, Smith SJ. Synaptic vesicle recycling in synapsin I knock-out mice. J Cell Biol. 1996;134:1219–27. https://doi.org/10.1083/jcb.134.5.1219.
42. Siksou L, Rostaing P, Lechaire J-P, Boudier T, Ohtsuka T, Fejtova A, et al. Three-dimensional architecture of presynaptic terminal cytomatrix. J Neurosci. 2007;27:6868–77. https://doi.org/10.1523/JNEUROSCI.1773-07.2007.
43. Burrone J, Li Z, Murthy VN. Studying vesicle cycling in presynaptic terminals using the genetically encoded probe synaptopHluorin. Nat Protoc. 2006;1:2970–8. https://doi.org/10.1038/nprot.2006.449.
44. Singla S, Kreitzer AC, Malenka RC. Mechanisms for synapse specificity during striatal long-term depression. J Neurosci. 2007;27:5260–4. https://doi.org/10.1523/JNEUROSCI.0018-07.2007.
45. Chevaleyre V, Takahashi KA, Castillo PE. Endocannabinoid-mediated synaptic plasticity in the CNS. Annu Rev Neurosci. 2006;29:37–76. https://doi.org/10.1146/annurev.neuro.29.051605.112834.
46. Atwood BK, Lovinger DM, Mathur BN. Presynaptic long-term depression mediated by Gi/o-coupled receptors. Trends Neurosci. 2014;37:663–73. https://doi.org/10.1016/j.tins.2014.07.010.
47. Puente N, Cui Y, Lassalle O, Lafourcade M, Georges F, Venance L, et al. Polymodal activation of the endocannabinoid system in the extended amygdala. Nat Neurosci. 2011;14:Article 12. https://doi.org/10.1038/nn.2974.
48. Fino E, Glowinski J, Venance L. Bidirectional activity-dependent plasticity at corticostriatal synapses. J Neurosci. 2005;25:11279–87. https://doi.org/10.1523/JNEUROSCI.4476-05.2005.
49. Njoo C, Agarwal N, Lutz B, Kuner R. The cannabinoid receptor CB1 interacts with the WAVE1 complex and plays a role in actin dynamics and structural plasticity in neurons. PLoS Biol. 2015;13:e1002286. https://doi.org/10.1371/journal.pbio.1002286.
50. Cesca F, Baldelli P, Valtorta F, Benfenati F. The synapsins: Key actors of synapse function and plasticity. Prog Neurobiol. 2010;91:313–48. https://doi.org/10.1016/j.pneurobio.2010.04.006.
51. Varma N, Brager DH, Morishita W, Lenz RA, London B, Alger B. Presynaptic factors in the regulation of DSI expression in hippocampus. Neuropharmacology. 2002;43:550–62. https://doi.org/10.1016/S0028-3908(02)00168-5.
52. Wilson RI, Kunos G, Nicoll RA. Presynaptic specificity of endocannabinoid signaling in the hippocampus. Neuron. 2001;31:453–62. https://doi.org/10.1016/S0896-6273(01)00372-5.
53. Li M, Ogilvie H, Ochala J, Artemenko K, Iwamoto H, Yagi N, et al. Aberrant post-translational modifications compromise human myosin motor function in old age. Aging Cell. 2015;14:228–35. https://doi.org/10.1111/acel.12307.
54. Chevaleyre V, Heifets BD, Kaeser PS, Südhof TC, Castillo PE. Endocannabinoid-mediated long-term plasticity requires cAMP/PKA signaling and RIM1α. Neuron. 2007;54:801–12. https://doi.org/10.1016/j.neuron.2007.05.020.
55. Mato S, Lafourcade M, Robbe D, Bakiri Y, Manzoni OJ. Role of the cyclic-AMP/PKA cascade and of P/Q-type Ca++ channels in endocannabinoid-mediated long-term depression in the nucleus accumbens. Neuropharmacology. 2008;54:87–94. https://doi.org/10.1016/j.neuropharm.2007.04.014.
56. Ritter SL, Hall RA. Fine-tuning of GPCR activity by receptor-interacting proteins. Nat Rev Mol Cell Biol. 2009;10:819–30. https://doi.org/10.1038/nrm2803.
57. Dong JM, Leung T, Manser E, Lim L. cAMP-induced morphological changes are counteracted by the activated RhoA small GTPase and the Rho kinase ROKalpha. J Biol Chem. 1998;273:22554–62. https://doi.org/10.1074/jbc.273.35.22554.
58. Jones SE, Palmer TM. Protein kinase A-mediated phosphorylation of RhoA on serine 188 triggers the rapid induction of a neuroendocrine-like phenotype in prostate cancer epithelial cells. Cell Signal. 2012;24:1504–14. https://doi.org/10.1016/j.cellsig.2012.03.018.
59. Oishi A, Makita N, Sato J, Iiri T. Regulation of RhoA signaling by the cAMP-dependent phosphorylation of RhoGDIα. J Biol Chem. 2012;287:38705–15. https://doi.org/10.1074/jbc.M112.401547.
60. Mukhopadhyay S, Howlett AC. CB1 receptor–G protein association. Eur J Biochem. 2001;268:499–505. https://doi.org/10.1046/j.1432-1327.2001.01810.x.
61. Glass M, Felder CC. Concurrent stimulation of cannabinoid CB1 and dopamine D2 receptors augments cAMP accumulation in striatal neurons: evidence for a Gs linkage to the CB1 receptor. J Neurosci. 1997;17:5327–33. https://doi.org/10.1523/JNEUROSCI.17-14-05327.1997.
62. Lauckner JE, Hille B, Mackie K. The cannabinoid agonist WIN55,212-2 increases intracellular calcium via CB1 receptor coupling to Gq/11 G proteins. Proc Natl Acad Sci USA. 2005;102:19144–9. https://doi.org/10.1073/pnas.0509588102.

63. Navarrete M, Araque A. Endocannabinoids mediate neuron-astrocyte communication. Neuron. 2008;57:883–93. https://doi.org/10.1016/j.neuron.2008.01.029.
64. Large M. The need for health warnings about cannabis and psychosis. Lancet Psychiatry. 2016;3:188–9. https://doi.org/10.1016/S2215-0366(15)00386-7.
65. Leterrier C, Potier J, Caillol G, Debarnot C, Rueda Boroni F, Dargent B. Nanoscale architecture of the Axon initial segment reveals an organized and robust scaffold. Cell Rep. 2015;13:2781–93. https://doi.org/10.1016/j.celrep.2015.11.051.
66. Schneider CA, Rasband WS, Eliceiri KW. NIH Image to ImageJ: 25 years of image analysis. Nat Methods. 2012;9:671–5. https://doi.org/10.1038/nmeth.2089.
67. Huang B, Wang W, Bates M, Zhuang X. Three-dimensional super-resolution imaging by stochastic optical reconstruction microscopy. Science. 2008;319:810–3. https://doi.org/10.1126/science.1153529.
68. Ovesný M, Křížek P, Borkovec J, Švindrych Z, Hagen GM. ThunderSTORM: A comprehensive ImageJ plug-in for PALM and STORM data analysis and super-resolution imaging. Bioinformatics. 2014;30:2389–90. https://doi.org/10.1093/bioinformatics/btu202.
69. Izeddin I, Boulanger J, Racine V, Specht CG, Kechkar A, Nair D, et al. Wavelet analysis for single molecule localization microscopy. Opt Express. 2012;20:2081–95. https://doi.org/10.1364/OE.20.002081.
70. Bleckert A, Photowala H, Alford S. Dual pools of actin at presynaptic terminals. J Neurophysiol. 2012;107:3479–92. https://doi.org/10.1152/jn.00789.2011.
71. Mochida S, Kobayashi H, Matsuda Y, Yuda Y, Muramoto K, Nonomura Y. Myosin II is involved in transmitter release at synapses formed between rat sympathetic neurons in culture. Neuron. 1994;13:1131–42. https://doi.org/10.1016/0896-6273(94)90051-5.

ACKNOWLEDGEMENTS

This work was supported by the MyoSynapse and NanoPaint grants of Paris Sciences et Lettres Research University and the Ecole des Neurosciences de Paris.

AUTHOR CONTRIBUTIONS

MHM: conceptualization, investigation, methodology, experimental analysis, biostatistical analysis, writing original draft, review & editing. MBE: conceptualization, investigation, methodology, biostatistical analysis. HX: investigation, experimental analysis, biostatistical analysis. YC: investigation, experimental analysis, biostatistical analysis. CL: methodology, review & editing. DZ conceptualization, investigation, methodology, review & editing, funding acquisition. LV: conceptualization, investigation, methodology, supervision, review & editing. ZL: conceptualization, investigation, methodology, supervision, funding acquisition, review & editing.

COMPETING INTERESTS

The authors declare no competing interests.

ADDITIONAL INFORMATION

Supplementary information The online version contains supplementary material available at https://doi.org/10.1038/s41398-024-03017-4.

Correspondence and requests for materials should be addressed to Zsolt Lenkei.

Reprints and permission information is available at http://www.nature.com/reprints

Publisher's note Springer Nature remains neutral with regard to jurisdictional claims in published maps and institutional affiliations.